Original Article

IDEAL-IQ measurement can distinguish dysplastic nodule from early hepatocellular carcinoma: a case-control study

Guangping Zheng[1#], Fangjun Wei[1#], Puxuan Lu[2], Gendong Yang[1], Cuizu Li[1], Chunming Lin[1], Yun Zhou[1], Yixin Chen[1], Jianing Tian[1], Xiaolei Wang[1], Linjing Wang[1], Wenhao Liu[1], Guangfeng Zhang[1], Qingxian Cai[1], Hua Huang[1], Yongxing Yun[1]^

[1]Department of Radiology, Shenzhen Third People's Hospital, Shenzhen, China; [2]Department of Radiology, Shenzhen Center for Chronic Disease Control, Shenzhen, China

Contributions: (I) Conception and design: G Zheng, F Wei, Y Yun; (II) Administrative support: P Lu, G Yang; (III) Provision of study materials or patients: C Qingxian, H Hua; (IV) Collection and assembly of data: C Li, C Lin, Y Zhou, Y Chen, J Tian, X Wang; (V) Data analysis and interpretation: L Wang, W Liu, G Zhang; (VI) Manuscript writing: All authors; (VII) Final approval of manuscript: All authors.

[#]These authors contributed equally to this work and should be considered as co-first authors.

Correspondence to: Yongxing Yun, MD. Department of Radiology, Shenzhen Third People's Hospital, No. 29 Buji Bulan Road, Longgang District, Shenzhen 518112, China. Email: 395942317@qq.com.

Background: Previous studies have confirmed that malignant transformation of dysplastic nodule (DN) into hepatocellular carcinoma (HCC) is accompanied by reduction of iron content in nodules. This pathological abnormality can serve as the basis for magnetic resonance imaging (MRI). This study was designed to identify the feasibility of iterative decomposition of water and fat with echo asymmetry and least squares estimation-iron quantitative (IDEAL-IQ) measurement to distinguish early hepatocellular carcinoma (eHCC) from DN.

Methods: We reviewed MRI studies of 35 eHCC and 23 DN lesions (46 participants with 58 lesions total, 37 males, 9 females, 31–80 years old). The exams include IDEAL-IQ sequence and 3.0T MR conventional scan [including T1-weighted imaging (T1WI), T2-weighted imaging (T2WI), diffusion-weighted imaging (DWI), and Gadopentic acid (Gd-GDPA)-enhanced]. Then, 3 readers independently diagnosed eHCC, DN, or were unable to distinguish eHCC from DN using conventional MRI (CMRI), and then assessed R2* value of nodules [R2* value represents the nodule iron content (NIC)] and R2* value of liver background [R2* value represents the liver background iron content (LBIC)] with IDEAL-IQ. Statistical analysis was conducted using the *t*-test for comparison of means, the Mann-Whitney test for comparison of medians, the chi-square test for comparison of frequencies, and diagnostic efficacy was evaluated by using receiver operating characteristic (ROC) curve.

Results: This study evaluated 35 eHCC participants (17 males, 6 females, 34–81 years old, nodule size: 10.5–27.6 mm, median 18.0 mm) and 23 DN participants (20 males, 3 females, 31–76 years old, nodule size: 16.30±4.095 mm). The NIC and ratio of NIC to LIBC (NIC/LBIC) of the eHCC group (35.926±12.806 sec^{-1}, 0.327±0.107) was lower than that of the DN group (176.635±87.686 sec^{-1}, 1.799±0.629) (P<0.001). Using NIC and NIC/LBIC to distinguish eHCC from DN, the true positive/false positive rates were 91.3%/94.3% and 87.0%/97.1%, respectively. The rates of CMRI, NIC and NIC/LBIC in diagnosis of eHCC were 77.1%, and 94.3%, 97.1%, respectively, and those of DN were 65.2%, 91.3%, and 87.0%, respectively. The diagnosis rate of eHCC and DN by CMRI was lower than that of NIC and NIC/LBIC (eHCC: P=0.03, 0.04, DN: P=0.02, 0.04).

^ ORCID: 0000-0002-6435-7661.

Conclusions: Using IDEAL-IQ measurement can distinguish DN from eHCC.

Keywords: Early hepatocellular carcinoma (eHCC); dysplastic nodule (DN); magnetic resonance imaging (MRI); iterative decomposition of water and fat with echo asymmetry and least squares estimation-iron quantitative (IDEAL-IQ)

Submitted Nov 09, 2023. Accepted for publication Mar 25, 2024. Published online Apr 22, 2024.
doi: 10.21037/qims-23-1593
View this article at: https://dx.doi.org/10.21037/qims-23-1593

Introduction

Hepatocellular carcinoma (HCC) is still one of the most common malignant tumors in worldwide. In 2020, HCC was the 6th most common cancer and the 3rd leading cause of cancer death in the world, with about 906,000 new cases and 830,000 deaths (1). At present, the definite image diagnosis of HCC is mainly based on contrast-enhanced imaging, however, there is still a portion of early hepatocellular carcinoma (eHCC) (approximately 23%) that is misdiagnosed as dysplastic nodule (DN) (2,3).

It is recognized that multistep hepatocarcinogenesis usually develops in the context of liver cirrhosis, and it is characterized by the following 3 phases: low- or high-grade DN, eHCC, and finally advanced HCC, and all these processes usually take from several years to more than 10 years. However, throughout the process, eHCC progresses quite rapidly to advanced HCC [approximately 3–18 months (median 12 months)] (4-7). Therefore, accurate diagnosis of eHCC is of great significance for clinical treatment. Although liver tissue biopsy is the gold standard for distinguishing DN and eHCC, it is an invasive examination and has contraindications such as large amounts of ascites, coagulation dysfunction, and tumor intra-abdominal implantation metastasis that limit its use. It is difficult to widely apply in clinical practice (8,9). Therefore, a non-invasive magnetic resonance imaging (MRI) examination method is necessary to effectively distinguish DN and eHCC.

Conventional MRI (CMRI) diagnosis of HCC and DN is mainly based on its morphology, signal changes, and hemodynamics. In general, DN shows high signal intensity on T1-weighted imaging (T1WI) and low signal intensity on T2-weighted imaging (T2WI), and gadoxetic acid-enhanced imaging in arterial phase can show hyperenhancement, whereas eHCC can also have the same appearance (10-12). Therefore, it is sometimes difficult to distinguish eHCC from DN. Although gadolinium ethoxybenzyl-diethylenetriaminepentaacetic acid (Gd-Eob-DTPA) enhanced can improve the sensitivity and specificity of eHCC diagnosis, there are still a portion of HCC that cannot be accurately diagnosed (12-14).

The development of DN into eHCC is accompanied by another pathophysiological change: decrease of iron content in nodules. Studies have confirmed that iron overload usually exists in regenerative nodule (RN), and when RN develops into DN, DN develops into eHCC, it is often accompanied by a gradual decrease of iron content in nodules, and this process is continuous (15-18). Therefore, we assume that the application of a non-invasive iron quantitative measurement technique to measure the iron content in the nodules can achieve the purpose of distinguishing eHCC from DN. In previous studies, qualitative or semi-quantitative MRI methods have been used to indirectly reflect the differences in endogenous iron content between eHCC and DN, but there has been no quantitative analysis of endogenous iron in nodules (19-23).

Iterative decomposition of water and fat with echo asymmetry and least squares estimation-iron quantitative (IDEAL-IQ) is an MRI method for quantitative measurement of iron and fat developed in recent years, which has been verified in phantoms, animal models, and patients (24-29). Therefore, it is feasible and meaningful to use IDEAL-IQ to measure the iron content of DN and eHCC.

The purpose of this study was to apply IDEAL-IQ to quantitatively measure the difference in iron content between eHCC and DN, and to evaluate its value for identification. We present this article in accordance with the STROBE reporting checklist (available at https://qims.amegroups.com/article/view/10.21037/qims-23-1593/rc).

Methods

Study population

This single-center retrospective case-control study was

approved by the Medical Ethics Committee of Shenzhen Third People's Hospital (approval No. 2022-035-02), and informed consent was provided by all participants. The study was conducted in accordance with the Declaration of Helsinki (as revised in 2013). We collected liver cirrhosis patients at the Department of Hepatology of the Shenzhen Third People's Hospital from 1 January 2019 to 31 December 2020. The inclusion criteria were as follows: (I) all participants were diagnosed with liver cirrhosis and intrahepatic nodules were found by any imaging examinations. (II) Maximum diameter of nodule <30 mm. (III) T1WI showed homogeneous hyperintensity or isointensity nodules. The exclusion criteria were as follows: (I) chronic liver disease due to vascular disorders or cirrhosis due to congenital hepatic fibrosis. (II) Liver paramagnetic substance deposition disease. (III) Without MRI examination or without IDEAL-IQ sequence examination. (IV) IDEAL-IQ sequence unable to locate nodules. (V) The nodules without final confirmation: (i) without histology confirmed and any imaging follow-up. (ii) Without histology confirmed, but the imaging follow-up could not be confirmed by Liver Imaging Reporting and Data System (LI-RADS; version 2018) (30) or digital subtraction angiography (DSA) imaging and transcatheter arterial chemoembolization (TACE) treatment.

MRI

All patients underwent MRI on the same scanner (Pioneer 3.0T; GE Healthcare, Chicago, IL, USA) using a 16-channel body coil, and images were post-processed on a multi-modality image review, comparison, and processing workstation (AW Volume Share 7 Workstation, GE Healthcare, USA). All examinations were performed with breath hold, and the MRI protocol included: (I) non-enhanced T1WI using liver acquisition with volume acceleration (LAVA-Flex): repetition time (TR)/echo time (TE), 4.5 ms/2 ms; flip angle, 12 degrees; slice thickness, 3 mm; intersection gap, 1 mm; bandwidth 142.86 kHz; field-of-view (FOV), 38 mm; number of excitations (NEX), 1. (II) T2WI using fast spin echo (FSE): TR/TE, 3,500–5,500 ms/70–90 ms; flip angle, 111 degrees; slice thickness, 7 mm; intersection gap, 1 mm; bandwidth 62.5 kHz; FOV, 38 mm; NEX, 1. (III) Diffusion-weighted imaging (DWI) using spin-echo echo-planar imaging (SEEPI): TR/TE, 2,350 ms/65 ms; slice thickness, 6 mm; intersection gap, 2 mm; bandwidth 250 kHz; FOV, 38 mm; NEX, 1. b values, 0 and 800 s/mm^2; (IV) IDEAL-IQ using LAVA: TR/TE, 6.2 ms/1 ms; 3 degrees; slice thickness, 5 mm; intersection gap, 1 mm; bandwidth 40 kHz; FOV, 40 mm; NEX, 0.75. (V) Dynamic contrast-enhanced MRI (DCE-MRI) using LAVA: TR/TE, 4.6 ms/2 ms; flip angle, 12 degrees; slice thickness, 3 mm; intersection gap, 1 mm; bandwidth 142.86 kHz; FOV, 38 mm; NEX, 1 (*Table 1*).

DCE-MRI used the contrast agent gadopentetate dimeglnmine (Magnevist; Bayer AG, Leverkusen, Germany), with an administered dose according to patient weight (0.2 mmol/kg; maximum dose, 20 mL) and injected at 2 mL/sec followed by a 15 mL saline flush at 2 mL/sec. Vascular phases images were acquired after administration of contrast agent, in late arterial phase (based on automated tracking technique), portal venous phase (50–60 sec), and delayed phase (3 min). DCE-MRI was performed after completion of IDEAL-IQ, T2WI, T1WI, and DWI. CMRI included T1WI, T2WI, DWI, and DCE-MRI. IDEAL-IQ included R2* mapping and proton density fat fraction (PDFF) mapping.

MRI analysis

MRI data were analyzed as follows: firstly, the nodules were divided into eHCC and DN groups according to the final clinical diagnosis. Secondly, CMRI images were independently read on the picture archiving and communication system (PACS) by 3 gastrointestinal radiologists (X.W., 14 years of work experience; G.Y., 26 years of work experience; Y.Z., 10 years of work experience) whom were blinded to clinical data, histology, and laboratory examinations. After reading the CMRI images, there were 3 diagnostic options to choose: (I) eHCC, (II) DN, (III) unable to distinguish eHCC from DN. The final MRI diagnoses were achieved by at least 2 radiologists' consistent diagnosis results. If the diagnosis results of at least 2 radiologists had not been achieved, option (III) was finally selected. Thirdly, another radiologist (W.L., 16 years of work experience) measured the R2* value of nodules [nodule iron content (NIC)]. In addition, in order to avoid the NIC from being affected by the background liver, we also measured the R2* value of the background liver [liver background iron content (LBIC)], and calculated the ratio (NIC/LBIC).

The measurement of NIC and LBIC was performed on AW Volume Share 7 Workstation. NIC measurement: Firstly, the nodules were accurately located on the R2* mapping with the help of CMRI images and PDFF mapping. Then, the ROI was manually drawn as much as

Table 1 MRI sequences and parameters

Parameters	T1WI (LAVA-Flex)	T2WI (FSE)	DWI (SE-EPI)	DCE-MRI (LAVA)	IDEAL-IQ
TR/TE (ms)	4.5/2	3,500–5,500/70–90	2,350/65	4.6/2	6.2/1
Flip angle (°)	12	111	–	12	3
Slice thickness (mm)	3	7	6	3	5
Intersection gap (mm)	1	1	2	1	–
Bandwidth (kHz)	142.86	62.5	250	142.86	111.11
Field-of-view (mm)	38	38	38	38	40
Number of excitations	1	2	1	1	0.75
b values (s/mm^2)	–	–	0/800	–	–

MRI, magnetic resonance imaging; T1WI, T1-weighted imaging; LAVA-Flex, liver acquisition with volume acceleration flex; T2WI, T2-weighted imaging; FSE, fast spin echo; DWI, diffusion-weighted imaging; SE-EPI, spin-echo echo-planar imaging; DCE-MRI, dynamic contrast-enhanced MRI; LAVA, liver acquisition with volume acceleration; IDEAL-IQ, iterative decomposition of water and fat with echo asymmetry and least squares estimation-iron quantification; TR, repetition time; TE, echo time.

possible to include most of the lesion on PDFF mapping, and the ROI was cloned from PDFF mapping to R2* mapping. LBIC measurement: 1 position was taken in the left lobe, right anterior lobe, and right posterior lobe of the liver, respectively on R2* mapping for measurement; the ROI area was about 300 mm^2, and avoiding blood vessels. The LBIC was taken as the average value of the3 measurements. The measured value was automatically generated by AW Volume Share 7 Workstation.

Nodule histology confirmation

These cases were rechecked by pathologists. The criteria to discriminate eHCC from DN included hepatocytic invasion of portal triads and septa (stromal invasion) (31).

Statistical analysis

Commercially available statistical software (SPSS 24.0, IBM, Armonk, NY, USA) was used for statistical analyses. Continuous variables with normal distribution were reported by the mean and standard deviation, and skew data by the median and range. Categorical variables were expressed in numbers and percentages.

The *t*-test, *t*'-test, or rank sum test were used to compare continuous variables.

The receiver operating characteristic (ROC) curve was used to evaluate the diagnostic efficacy for NIC and NIC/LBIC, and the cut-off value was estimated by the Youden index (32). Chi-square test was used for pairwise comparison of the rates between CMRI, NIC, and NIC/LBIC (categorical variables).

Results

Characteristics of study participants

A total of 167 participants were screened and 121 were excluded. According to exclusion criteria, participants with liver paramagnetic substance deposition disease (n=15) (4 with hemochromatosis, 9 with Wilson disease, and 2 with long-term blood transfusion products), with chronic liver disease due to vascular disorders or cirrhosis due to congenital hepatic fibrosis (n=9) (9 with Budd-Chiari), Without MRI examination or without IDEAL-IQ sequence examination (n=28) (19 without MRI examination, 9 without IDEAL-IQ), with IDEAL-IQ unable to locate the nodules (n=17), and nodules without final confirmation (n=52) were excluded. Finally, 46 participants (37 males, 9 females, 52.4±13.6 years) were included in the study (58 nodules in total met the inclusion and exclusion criteria: 38 with single nodule, 4 with 2 nodules, and 4 with 3 nodules) (*Figure 1*). Among these 46 participants, 19 underwent only 1 MRI examination, 11 underwent 2 MRI examinations (interval between the 2 examinations ≥3 months), and 16 underwent more than 2 MRI examinations. Among these 58 nodules, 49 were confirmed by histology [surgical resection or needle biopsy, HCC (n=26), DN (n=23)], and 9 were confirmed by the imaging follow-up (LI-RADS version 2018, LR-5 categorization or

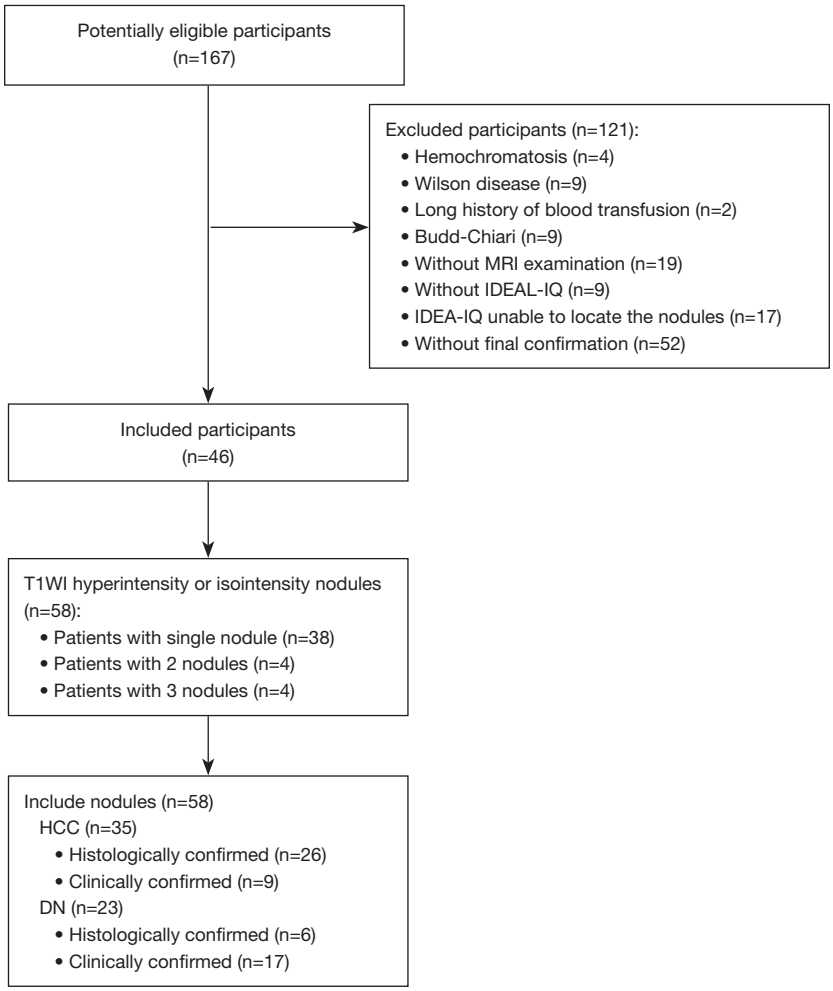

Figure 1 Flowchart of patient selection. MRI, magnetic resonance imaging; IDEAL-IQ, iterative decomposition of water and fat with echo asymmetry and least squares estimation-iron quantification; T1WI, T1-weighted imaging; HCC, hepatocellular carcinoma; DN, dysplastic nodule.

higher), and DSA imaging showed tumor staining; TACE treatment showed iodine deposition within the nodule [HCC (n=9)].

Clinical characteristics of the study participants are reported in the *Table 2*. The mean time interval between the date of MRI examination and the date of clinical characteristics recording were 11.8±4.8 days.

Characteristic analysis of eHCC and DN

The characteristics of eHCC and DN are summarized in *Table 3*, and the NIC and NIC/LBIC data distributions plots are summarized in *Figure 2*. The maximum diameter of nodules, LBIC, NIC, and LIC/LBIC of eHCC and DN were compared. There were no differences in the maximum diameter and LBIC between eHCC [n=35, maximum diameter = (10.5–27.6 mm, median 18.0 mm), LBIC = (54.2–360.0 sec^{-1}, median 103.3 sec^{-1})] and DN [n=23, maximum diameter = (16.30±4.095 mm), LBIC = (30.6–744.9 sec^{-1}, median 80.20 sec^{-1})], P=0.11, P=0.79, respectively. The NIC and LIC/LBIC of eHCC [NIC = (35.926±12.806 sec^{-1}), NIC/LBIC = (0.327±0.107)] were lower than DN [NIC = (176.635±87.686 sec^{-1}), LIC/LBIC = (1.799±0.629)], P<0.001, P<0.001, respectively.

Image features of eHCC and DN on R2 Map*

In these cases, eHCC showed T1WI hyperintensity and T2WI slight hyperintensity (*Figure 3A,3B*), DWI (b=800 s/mm^2) showed mild hyperintensity or isointensity

Table 2 Clinical characteristics of the study participants (N=46)

Characteristics	HCC (N=35, 60.3%)	DN (N=23, 39.7%)	P value
Age, years	51 (34–81)	51 (31–76)	0.39
Gender, N (%)			
Male	32 (69.6)	5 (10.9)	0.03
Female	1 (2.2)	8 (17.4)	0.03
Personal disease history, N (%)			
Hepatitis B cirrhosis	32 (69.6)	8 (17.4)	0.29
Hepatitis C cirrhosis	3 (6.5)	0 (0.0)	<0.01
Alcoholic cirrhosis	0 (0.0)	2 (4.3)	<0.01
Autoimmune hepatitis cirrhosis	0 (0.0)	1 (2.2)	<0.01
Duration of cirrhosis, months	52 (36–96)	32 (20–62)	0.02
Clinical symptoms and signs, N (%)			
Abdominal pain	24 (52.1)	6 (13.0)	0.65
Fatigue	31 (67.4)	8 (17.4)	0.63
Jaundice	29 (63.0)	4 (8.7)	0.22
Gastrointestinal bleeding	12 (26.1)	2 (4.3)	0.10
Splenomegaly	35 (76.1)	11 (23.9)	0.53
Ascites	14 (30.4)	7 (15.2)	0.62
Liver palm	33 (71.7)	10 (21.7)	0.33
Spider nevus	33 (71.7)	10 (21.7)	0.33
Epigastric mass	0 (0.0)	0 (0.0)	
Laboratory investigations			
GGT ($U \times L^{-1}$)	90±12 (47–234)	23±11 (9–56)	0.23
ALT ($U \times L^{-1}$)	93±19 (33–362)	49±15 (13–86)	0.33
AST ($U \times L^{-1}$)	78±13 (28–198)	86±19 (38–124)	0.28
AFP ($ng \times L^{-1}$)	62.9 (0.9–1,012.9)	4.3 (2.0–38.5)	<0.01
Liver function (Child-Pugh), N (%)			
Grade A	1 (2.2)	5 (10.9)	0.02
Grade B	13 (28.3)	5 (10.9)	0.03
Grade C	21 (45.7)	1 (2.2)	0.03
MRI examination, N			
Only 1 examination	15	4	
2 examinations	7	4	
More than 2 examinations	11	5	

For continuous variables, normal distribution data are represented as mean ± SD (range), and skew distribution data are represented as median (range). For categorical variables, data are absolute value. HCC, hepatocellular carcinoma; DN, dysplastic nodule; GGT, gamma glutamyl transpeptidase; ALT, alanine aminotransferase; AST, aspartate transaminase; AFP, alpha-fetoprotein; MRI, magnetic resonance imaging; SD, standard deviation.

Table 3 Comparison of DN and eHCC features

Characteristics	eHCC		DN		P value (HCC *vs.* DN)
	Nodule measurement	P value	Nodule measurement	P value	
Nodule maximum diameter (mm)	△18.0 (10.5–27.6)	0.01	°16.30±4.095 (14.53–18.08)	0.20	0.11
Nodule R2* value (sec^{-1}) (NIC)	°35.926±12.806 (13.5–89.2)	0.20	°176.635±87.686 (53.2–378.0)	0.12	<0.001
Background liver R2 value (sec^{-1}) (LBIC)	△103.3 (54.2–360.0)	0.02	△80.20 (30.6–744.9)	<0.001	0.79
NIC/LBIC	°0.327±0.107 (0.087–0.618)	0.20	°1.799±0.629 (0.353–3.246)	0.18	<0.001

Data (△) are median (range), data (°) are mean ± SD (range). The P value in the third and the fifth column of the table represents the P value of normality test and homogeneity of variance test. The P value in the sixth column of the table represents the P value of DN and eHCC comparison. P<0.05 is considered to indicate statistical significance. DN, dysplastic nodule; eHCC, early hepatocellular carcinoma; HCC, hepatocellular carcinoma; NIC, nodule iron content; LBIC, liver background iron content; NIC/LBIC, ratio of nodule iron content to liver background iron content; SD, standard deviation.

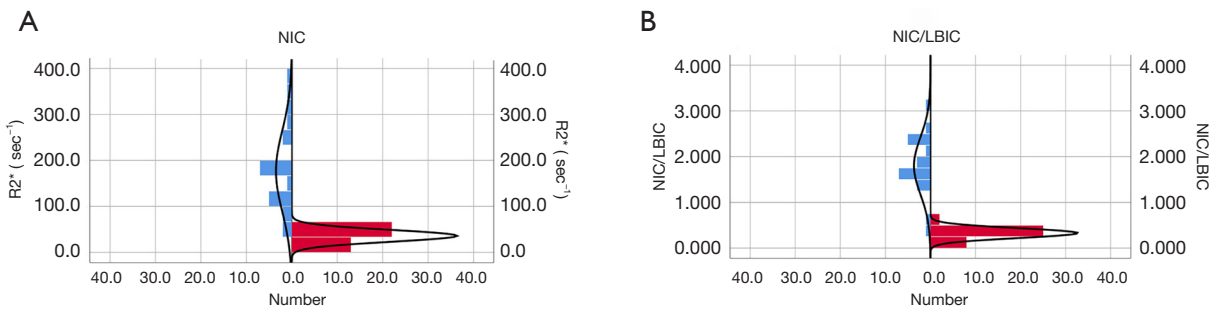

Figure 2 Comparison of R2* values (NIC) and NIC/LBIC in eHCC and DN. (A) The R2* value of eHCC (red bars) (35.926±12.806 sec^{-1}) was lower than that of DN (blue bars) (176.635±87.686 sec^{-1}), P<0.001. (B) The NIC/LBIC of eHCC (red bars) (0.327±0.107) was lower than that of DN (blue bars) (1.799±0.629), P<0.001. NIC, nodule iron content; LBIC, liver background iron content; NIC/LBIC, ratio of nodule iron content to liver background iron content-iron quantification; eHCC, early hepatocellular carcinoma; DN, dysplastic nodule.

(*Figure 3C*). DEC-MRI manifestation was as follows: arterial phase mild hyperenhancement (*Figure 3D*), and washout appearance in portal venous phase and delayed phase (*Figure 3E,3F*). With Gd-Eob-DTPA enhancement, eHCC and DN showed hepatobiliary phase (10, 20 min) hypointensity (*Figure 3G,3H*). Compared with CMRI images, the outline of the eHCC on R2* mapping was more blurred. It tended to show slightly hyperintensity in PDFF mapping (*Figure 3I*), yet low R2* value in R2* mapping (*Figure 3J*). Tumor surgical excision specimen (*Figure 3K*) and histological images eventually confirmed eHCC (hematoxylin eosin staining, ×10) (*Figure 3L*).

The imaging findings of DN were similar to those of eHCC. DN showed T1WI hyperintensity and T2WI slight hyperintensity (*Figure 4A,4B*), DWI (b=800 s/mm^2) showed mild hyperintensity or isointensity (*Figure 4C*). DEC-MRI manifestation was: arterial phase mild hyperenhancement (*Figure 4D*), and washout appearance in portal venous phase and delayed phase (*Figure 4E,4F*). Compared with CMRI images, the outline of the DN on R2* mapping was also more blurred. It tended to show slightly hyperintensity in PDFF mapping (*Figure 4G*), yet high R2* value in R2* mapping (*Figure 4H*). With Gd-Eob-DTPA enhancement, DN also showed hepatobiliary phase (10, 20 min) hypointensity (*Figure 4I,4J*).

DSA examination of DN showed no tumor staining (*Figure 4K*). Histological images eventually confirmed DN (needle biopsy, hematoxylin eosin staining, ×20) (*Figure 4L*).

NIC and NIC/LBIC diagnostic efficacy evaluation

The ROC curve was used to evaluate the diagnostic efficacy of NIC and NIC/LBIC (*Figure 5*), which showed that NIC and NIC/LBIC were effective in differential diagnosis of eHCC and DN. The area under the curve (AUC) was 0.979 and 0.923 (P<0.001), and the cutoff value was 71.45 sec^{-1}

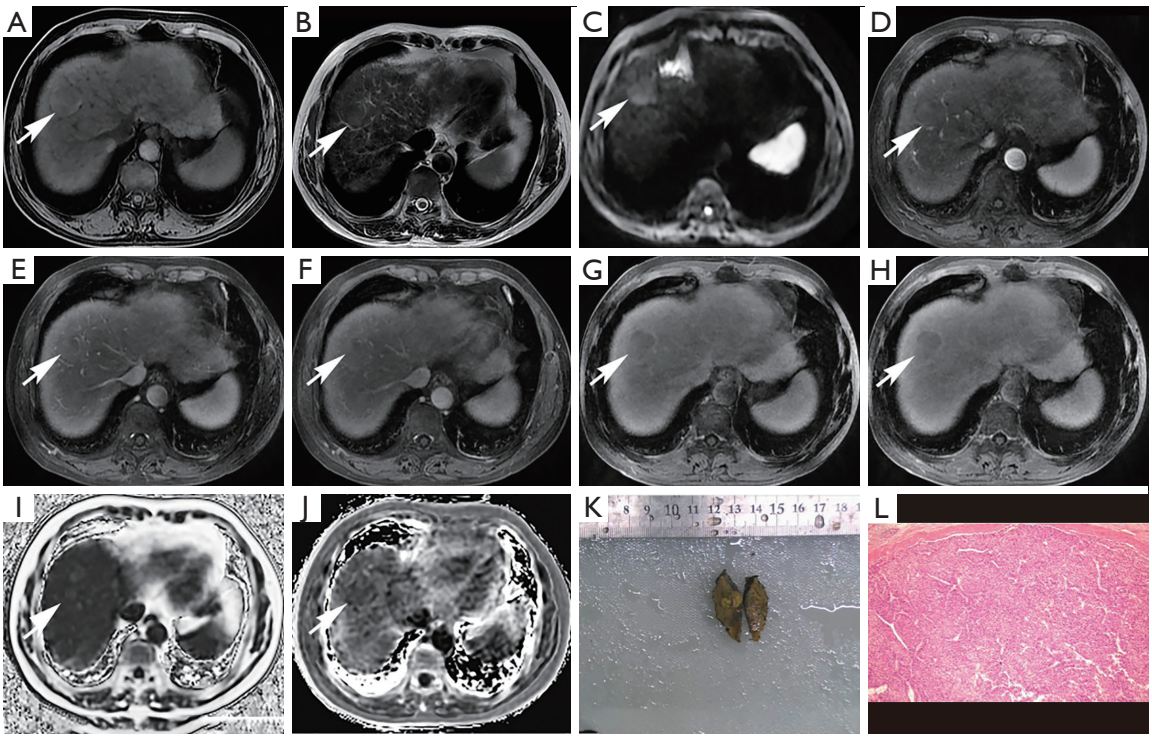

Figure 3 MR images in a 52-year-old man with HCC (white arrow). Mass in segment VIII with T1WI hyperintensity (A), T2WI slightly hyperintensity (B) and DWI (b=800 s/mm^2) hyperintensity (C). DCE-MRI (D-F): arterial phase mild hyperenhancement (D), washout appearance in portal venous phase (E) and delayed phase (F). In this case, 2 of the 3 radiologists diagnosed eHCC based on CMRI. Then, this patient also underwent Gadoxetic acid disodium (Gd-Eob-DTPA) enhancement: hepatobiliary phase in 10 minutes (G) and 20 minutes (H) showed mass hypointensity. IDEAL-IQ (I,J): the mass showed blur and slightly hyperintensity in PDFF mapping (I), yet low R2* value in R2* mapping (R2* value =49.523 sec^{-1}) (J). Tumor surgical excision specimen (K). Histological images (hematoxylin and eosin staining, ×10) (L). MR, magnetic resonance; HCC, hepatocellular carcinoma; T1WI, T1-weighted imaging; T2WI, T2-weighted imaging; DWI, diffusion-weighted imaging; DCE-MRI, dynamic contrast-enhanced MRI; eHCC, early hepatocellular carcinoma; CMRI, conventional MRI; Gd-Eob-DTPA, gadolinium ethoxybenzyl-diethylenetriaminepentaacetic acid; IDEAL-IQ, iterative decomposition of water and fat with echo asymmetry and least squares estimation-iron quantification; PDFF, proton density fat fraction; MRI, magnetic resonance imaging.

and 1.275, respectively. The true positive rate was 91.3%, 94.3%, and the false positive rate was 87.0%, 97.1%, respectively.

Comparison of diagnostic accuracy

The diagnostic accuracy of CMRI, NIC, and NIC/LBIC in the diagnosis of eHCC and DN were compared (*Table 4*). The rates of CMRI, NIC, and NIC/LBIC in the diagnosis of eHCC were 77.1%, 94.3%, and 97.1%, respectively, and those of DN were 65.2%, 91.3%, and 87.0%, respectively. The diagnosis rate of eHCC and DN by CMRI were lower than NIC and NIC/LBIC (eHCC: P=0.03, 0.04, DN: P=0.02, 0.04), and there were no differences between NIC and NIC/LBIC (eHCC: P=0.16, DN: P=0.06).

Discussion

In this retrospective case-control study of 58 lesions, we found that it was feasible to distinguish eHCC from DN by IDEAL-IQ iron quantitative measurement. We observed that the NIC and NIC/LBIC of eHCC were lower than that of DN. Moreover, the application of NIC and NIC/LBIC in the differential diagnosis of eHCC and DN showed a good diagnostic efficiency. In addition, we also compared the diagnostic accuracy of IDEAL-IQ and CMRI, and found that IDEAL-IQ has better differential ability. Therefore, our study confirmed that IDEAL-IQ can

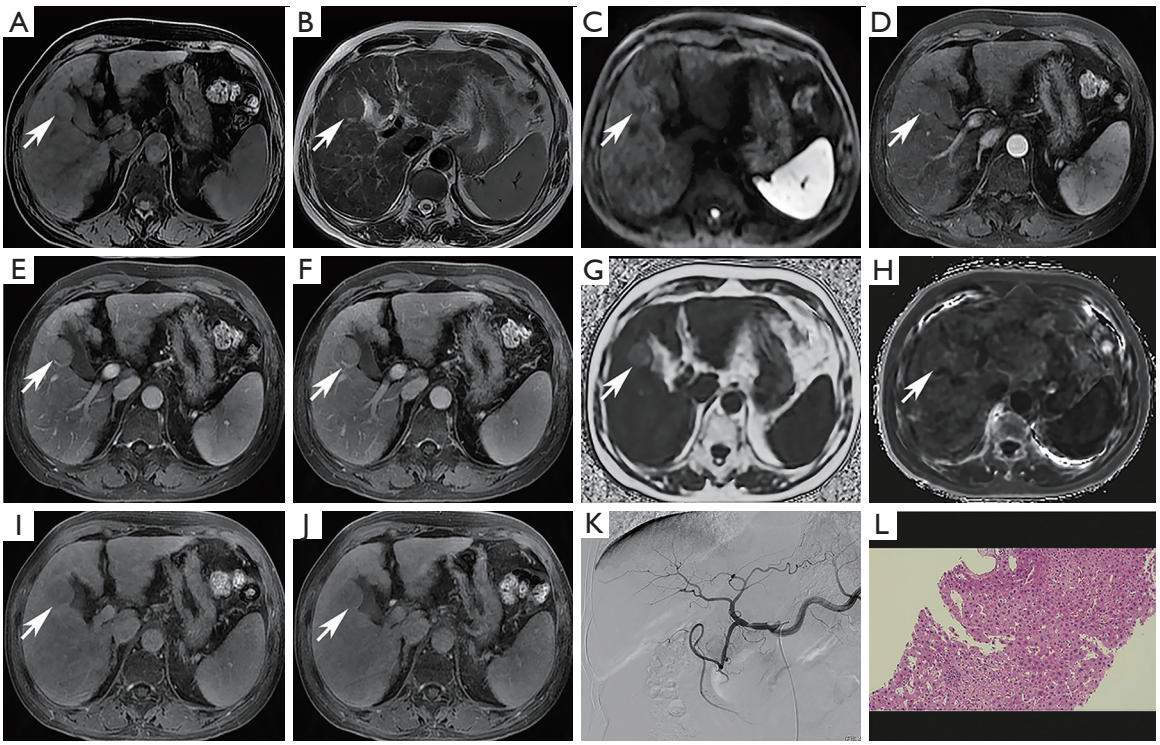

Figure 4 MR images in a 49-year-old man with DN (white arrow). Nodule in segment V with T1WI slightly hyperintensity (A), T2WI slightly hyperintensity (B), and DWI (b=800) was blurred (C). DCE-MRI (D-F): arterial phase mild hyperenhancement (D), washout appearance in portal venous phase (E) and delayed phase (F). In this case, all 3 radiologists diagnosed eHCC based on CMRI. IDEAL-IQ (G,H): the nodule showed hyperintensity in PDFF mapping (G) and high R2* value in R2* mapping (R2* value =76.500 sec^{-1}) (H). This patient also underwent Gadoxetic acid disodium (Gd-Eob-DTPA) enhancement: hepatobiliary phase in 10 minutes (I) and 20 minutes (J) showed nodule hypointensity. DSA examination showed no tumor staining (K). Histological image (needle biopsy, hematoxylin and eosin staining, ×20) (L). MR, magnetic resonance; DN, dysplastic nodule; T1WI, T1-weighted imaging; T2WI, T2-weighted imaging; DWI, diffusion-weighted imaging; DCE-MRI, dynamic contrast-enhanced MRI; eHCC, early hepatocellular carcinoma; CMRI, conventional MRI; IDEAL-IQ, iterative decomposition of water and fat with echo asymmetry and least squares estimation-iron quantification; Gd-Eob-DTPA, gadolinium ethoxybenzyl-diethylenetriaminepentaacetic acid; MRI, magnetic resonance imaging.

be used to distinguish eHCC from DN.

Previous studies have provided strong evidence that the occurrence of HCC is related to the decrease of endogenous iron deposition in nodules (15,16,31,33). However, these studies have limitations. In these studies, it was observed that the signals of T2WI* or R2* of eHCC were different from those of DN, but there was no quantitative analysis of endogenous iron in nodules. The reduction of iron content in nodules is a continuous process; eHCC is different from advanced HCC, in which advanced HCC shows the endogenous iron wash-out, whereas eHCC often shows a small amount of endogenous iron wash-out (33). In most cases, the endogenous iron content of eHCC is similar to thast of DN. Therefore, it is difficult to distinguish eHCC from DN because of their similar signal in sometimes (*Figures 3A*,*3B*,*4A*,*4B*). Our study used IDEAL-IQ for iron quantitative analysis of nodules, which can better reflect the difference of endogenous iron between eHCC and DN, to achieve the purpose of distinguishing eHCC from DN. In this study, both NIC and NIC/LIBC were able to distinguish eHCC and DN. It is known that patients with cirrhosis are also accompanied by liver iron deposition, and LIBC may increase the NIC measurement. NIC/LIBC can eliminate the effect of LIBC on NIC, and NIC/LIBC may be more reasonable than NIC for patients with severe liver iron deposition, which needs further study.

At present, it is still challenging to distinguish eHCC from DN by conventional non-invasive methods (such

as CMRI and Gd-EOB-DTPA MRI). The reason is that the MRI signal and enhancement features of DN and eHCC overlap: DN usually shows T1WI hyperintensity and T2WI isointensity or hypointensity, but eHCC can also show these characteristics (34). In DCE-MRI images, the manifestations of DN and eHCC can also be very similar, both of them can show hyperenhancement in the arterial phase and persistent hyperenhancement in the portal venous phase, especially high-grade dysplastic nodules (HGDN) are sometimes difficult to distinguish from eHCC (34). Although Gd-EOB-DTPA-enhanced MRI can improve the diagnostic accuracy, it is sometimes difficult to distinguish eHCC from DN, because a portion of eHCC show hyperintensity and DN show hypointensity in the hepatobiliary phase, which are different from the common manifestations of HCC and DN in hepatobiliary phase (35). Our research also found the above phenomenon (*Figures 3*,*4*). In view of this, our study screened these kinds of nodules that were difficult to differentiate and used IDEAL-IQ for differentiation. Interestingly, we found that the diagnostic accuracy of IDEAL-IQ was better than that of CMRI.

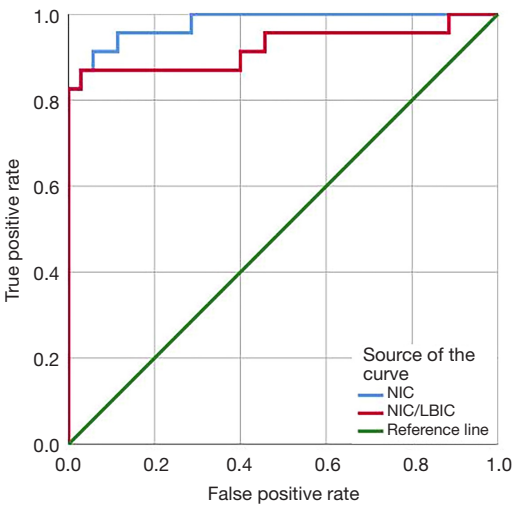

Figure 5 ROC curves of NIC and NIC/LBIC distinguish HCC from DN. The AUC was 0.979 (95% CI: 0.949–0.992) and 0.923 (95% CI: 0.831–0.954) (P<0.01), and the cutoff value was 71.45 sec^{-1} and 1.275, respectively. The true positive rate was 91.3%, 94.3%, and the false positive rate was 87.0%, 97.1%, respectively. NIC, nodule iron content; LBIC, liver background iron content; NIC/LBIC, ratio of nodule iron content to liver background iron content; ROC, receiver operating characteristic; HCC, hepatocellular carcinoma; DN, dysplastic nodule; AUC, area under the curve; CI, confidence interval.

IDEAL-IQ has been shown to be highly reliable in patients with iron overload (24,25). It is often used to evaluate liver iron overload in patients with liver cirrhosis and hemochromatosis, but it has not been found to study the endogenous iron content of DN and HCC. Our study found that when CMRI is difficult to distinguish eHCC from DN, the assistance of IDEAL-IQ can improve the accuracy of diagnosis. However, R2* mapping of IDEAL-IQ has an obvious disadvantage, that is, the outline of the nodule is blurred, so it is difficult to accurately locate the lesions on the image. Therefore, it is necessary to locate the lesions with the help of CMRI. In this study, there were 17 cases in which the nodules were clearly displayed on the CMRI images, but failed to be displayed on the IDEAL-IQ images. Even with the help of CMRI, the nodules could also not be located, so that ROI could not be drawn. We found that the 46 cases of IDEAL-IQ images included in the study had no motion artifacts, whereas the 17 cases excluded had motion artifacts and could not be displayed and located. Therefore, we estimated that motion artifacts may be the main reason for failure to display the lesion, and slice thickness may also be one of the reasons affecting the display of the lesion. If motion artifacts are suppressed and slice thickness is reduced, the lesions may be better displayed. Recently, developed complex chemical

Table 4 Comparison of diagnostic rate between CMRI, NIC and NIC/NIBC

Diagnosis results	CMRI	NIC	NIC/LBIC	P^1	P^2	P^3
eHCC (n=35), n (%)	27 (77.1)	33 (94.3)	34 (97.1)	0.03	0.04	0.16
DN (n=23), n (%)	15 (65.2)	21 (91.3)	20 (87)	0.02	0.04	0.06

Data outside brackets are diagnostic accuracy. P<0.05 is considered to indicate statistical significance. [1], statistical difference between CMRI and NIC; [2], statistical difference between CMRI and NIC/LBIC; [3], statistical difference between NIC and NIC/LBIC. CMRI, conventional MRI; NIC, nodule iron content; NIC/LBIC, ratio of nodule iron content to liver background iron content; LBIC, liver background iron content; eHCC, early hepatocellular carcinoma; DN, dysplastic nodule; MRI, magnetic resonance imaging.

shift encoded (CSE)-MRI techniques that use both the magnitude and phase of the gradient echo (GRE) signal enable to obtain better R2* mapping images, such that lesions may be clearly displayed and R2* values can be measured without the help of CMRI (36).

Our study had some limitations. Firstly, this was a single center retrospective case-control study with a small sample size. Secondly, we only included T1WI high signal nodules for study, and other T1WI signal nodules might also benefit from the use of this method. In addition, the precision or repeatability of the IDEAL-IQ had not been evaluated. In conclusion, our study findings demonstrated that the application of IDEAL-IQ can distinguish eHCC from DN, which can improve the diagnostic accuracy.

Conclusions

IDEAL-IQ is an MRI method for the quantitative measurement of iron and fat. Our findings confirm that IDEAL-IQ can be used to differentiate DN from eHCC, which have important clinical significance and provide a new method for following researchers.

Acknowledgments

Funding: This work was supported by Shenzhen High-level Hospital Construction Fund (No. G2022108).

Footnote

Reporting Checklist: The authors have completed the STROBE reporting checklist. Available at https://qims.amegroups.com/article/view/10.21037/qims-23-1593/rc

Conflicts of Interest: All authors have completed the ICMJE uniform disclosure form (available at https://qims.amegroups.com/article/view/10.21037/qims-23-1593/coif). All authors report that this study received funding from Shenzhen High-level Hospital Construction Fund (No. G2022108). The authors have no other conflicts of interest to declare.

Ethical Statement: The authors are accountable for all aspects of the work in ensuring that questions related to the accuracy or integrity of any part of the work are appropriately investigated and resolved. This study was approved by the Medical Ethics Committee of Shenzhen Third People's Hospital (approval No. 2022-035-02), and informed consent was provided by all the patients. The study was conducted in accordance with the Declaration of Helsinki (as revised in 2013).

References

1. Sung H, Ferlay J, Siegel RL, Laversanne M, Soerjomataram I, Jemal A, Bray F. Global Cancer Statistics 2020: GLOBOCAN Estimates of Incidence and Mortality Worldwide for 36 Cancers in 185 Countries. CA Cancer J Clin 2021;71:209-49.
2. van der Pol CB, McInnes MDF, Salameh JP, Levis B, Chernyak V, Sirlin CB, et al. CT/MRI and CEUS LI-RADS Major Features Association with Hepatocellular Carcinoma: Individual Patient Data Meta-Analysis. Radiology 2022;302:326-35.
3. Yang JD, Heimbach JK. New advances in the diagnosis and management of hepatocellular carcinoma. BMJ 2020;371:m3544.
4. Takayama T, Makuuchi M, Hirohashi S, Sakamoto M, Okazaki N, Takayasu K, Kosuge T, Motoo Y, Yamazaki S, Hasegawa H. Malignant transformation of adenomatous hyperplasia to hepatocellular carcinoma. Lancet 1990;336:1150-3.
5. Sakamoto M, Hirohashi S, Shimosato Y. Early stages of multistep hepatocarcinogenesis: adenomatous hyperplasia and early hepatocellular carcinoma. Hum Pathol 1991;22:172-8.
6. Villanueva A. Hepatocellular Carcinoma. N Engl J Med 2019;380:1450-62.
7. Di Tommaso L, Sangiovanni A, Borzio M, Park YN, Farinati F, Roncalli M. Advanced precancerous lesions in the liver. Best Pract Res Clin Gastroenterol 2013;27:269-84.
8. Russo FP, Imondi A, Lynch EN, Farinati F. When and how should we perform a biopsy for HCC in patients with liver cirrhosis in 2018? A review. Dig Liver Dis 2018;50:640-6.
9. Pang EH, Harris AC, Chang SD. Approach to the Solitary

Liver Lesion: Imaging and When to Biopsy. Can Assoc Radiol J 2016;67:130-48.
10. Willatt JM, Hussain HK, Adusumilli S, Marrero JA. MR Imaging of hepatocellular carcinoma in the cirrhotic liver: challenges and controversies. Radiology 2008;247:311-30.
11. Sartoris R, Gregory J, Dioguardi Burgio M, Ronot M, Vilgrain V. HCC advances in diagnosis and prognosis: Digital and Imaging. Liver Int 2021;41 Suppl 1:73-7.
12. Inoue T, Kudo M, Komuta M, Hayaishi S, Ueda T, Takita M, Kitai S, Hatanaka K, Yada N, Hagiwara S, Chung H, Sakurai T, Ueshima K, Sakamoto M, Maenishi O, Hyodo T, Okada M, Kumano S, Murakami T. Assessment of Gd-EOB-DTPA-enhanced MRI for HCC and dysplastic nodules and comparison of detection sensitivity versus MDCT. J Gastroenterol 2012;47:1036-47.
13. Wang YC, Chou CT, Lin CP, Chen YL, Chen YF, Chen RC. The value of Gd-EOB-DTPA-enhanced MR imaging in characterizing cirrhotic nodules with atypical enhancement on Gd-DTPA-enhanced MR images. PLoS One 2017;12:e0174594.
14. Ichikawa T, Sano K, Morisaka H. Diagnosis of Pathologically Early HCC with EOB-MRI: Experiences and Current Consensus. Liver Cancer 2014;3:97-107.
15. Kew MC. Hepatic iron overload and hepatocellular carcinoma. Liver Cancer 2014;3:31-40.
16. Haider MB, Al Sbihi A, Chaudhary AJ, Haider SM, Edhi AI. Hereditary hemochromatosis: Temporal trends, sociodemographic characteristics, and independent risk factor of hepatocellular cancer - nationwide population-based study. World J Hepatol 2022;14:1804-16.
17. Pecorelli A, Franceschi P, Braccischi L, Izzo F, Renzulli M, Golfieri R. MRI Appearance of Focal Lesions in Liver Iron Overload. Diagnostics (Basel) 2022.
18. Asare GA, Paterson AC, Kew MC, Khan S, Mossanda KS. Iron-free neoplastic nodules and hepatocellular carcinoma without cirrhosis in Wistar rats fed a diet high in iron. J Pathol 2006;208:82-90.
19. Taylor BA, Loeffler RB, Song R, McCarville MB, Hankins JS, Hillenbrand CM. Simultaneous field and R2 mapping to quantify liver iron content using autoregressive moving average modeling. J Magn Reson Imaging 2012;35:1125-32.
20. Hernando D, Levin YS, Sirlin CB, Reeder SB. Quantification of liver iron with MRI: state of the art and remaining challenges. J Magn Reson Imaging 2014;40:1003-21.
21. Kudo M. Multistep human hepatocarcinogenesis: correlation of imaging with pathology. J Gastroenterol 2009;44 Suppl 19:112-8.
22. Golfeyz S, Lewis S, Weisberg IS. Hemochromatosis: pathophysiology, evaluation, and management of hepatic iron overload with a focus on MRI. Expert Rev Gastroenterol Hepatol 2018;12:767-78.
23. Li RK, Palmer SL, Zeng MS, Qiang JW, Chen F, Rao SX, Chen LL, Dai YM. Detection of Endogenous Iron Reduction during Hepatocarcinogenesis at Susceptibility-Weighted MR Imaging: Value for Characterization of Hepatocellular Carcinoma and Dysplastic Nodule in Cirrhotic Liver. PLoS One 2015;10:e0142882.
24. Eskreis-Winkler S, Corrias G, Monti S, Zheng J, Capanu M, Krebs S, Fung M, Reeder S, Mannelli L. IDEAL-IQ in an oncologic population: meeting the challenge of concomitant liver fat and liver iron. Cancer Imaging 2018;18:51.
25. Yu H, Shimakawa A, McKenzie CA, Brodsky E, Brittain JH, Reeder SB. Multiecho water-fat separation and simultaneous R2* estimation with multifrequency fat spectrum modeling. Magn Reson Med 2008;60:1122-34.
26. Li Y, Xiong Y, Hou B, Liu C, Wang J, Morelli JN, Hu S, Zhang Y, Sun D, Li X. Detection of erosions and fat metaplasia of the sacroiliac joints in patients with suspected sacroiliitis using a chemical shift-encoded sequence (IDEAL-IQ). Eur J Radiol 2023;158:110641.
27. Serai SD, Dillman JR, Trout AT. Proton Density Fat Fraction Measurements at 1.5- and 3-T Hepatic MR Imaging: Same-Day Agreement among Readers and across Two Imager Manufacturers. Radiology 2017;284:244-54.
28. Qi Q, Weinstock AK, Chupetlovska K, Borhani AA, Jorgensen DR, Furlan A, Behari J, Molinari M, Ganesh S, Humar A, Duarte-Rojo A. Magnetic resonance imaging-derived proton density fat fraction (MRI-PDFF) is a viable alternative to liver biopsy for steatosis quantification in living liver donor transplantation. Clin Transplant 2021;35:e14339.
29. Idilman IS, Tuzun A, Savas B, Elhan AH, Celik A, Idilman R, Karcaaltincaba M. Quantification of liver, pancreas, kidney, and vertebral body MRI-PDFF in non-alcoholic fatty liver disease. Abdom Imaging 2015;40:1512-9.
30. Chernyak V, Fowler KJ, Kamaya A, Kielar AZ, Elsayes KM, Bashir MR, Kono Y, Do RK, Mitchell DG, Singal AG, Tang A, Sirlin CB. Liver Imaging Reporting and Data System (LI-RADS) Version 2018: Imaging of Hepatocellular Carcinoma in At-Risk Patients. Radiology 2018;289:816-30.
31. Takayama T, Makuuchi M, Kojiro M, Lauwers GY, Adams RB, Wilson SR, Jang HJ, Charnsangavej C, Taouli B.

Early hepatocellular carcinoma: pathology, imaging, and therapy. Ann Surg Oncol 2008;15:972-8.
32. Hughes G. Youden's index and the weight of evidence. Methods Inf Med 2015;54:198-9.
33. Honda H, Kaneko K, Kanazawa Y, Hayashi T, Fukuya T, Matsumata T, Maeda T, Masuda K. MR imaging of hepatocellular carcinomas: effect of Cu and Fe contents on signal intensity. Abdom Imaging 1997;22:60-6.
34. Rhee H, Kim MJ, Park YN, Choi JS, Kim KS. Gadoxetic acid-enhanced MRI findings of early hepatocellular carcinoma as defined by new histologic criteria. J Magn Reson Imaging 2012;35:393-8.
35. Renzulli M, Biselli M, Brocchi S, Granito A, Vasuri F, Tovoli F, Sessagesimi E, Piscaglia F, D'Errico A, Bolondi L, Golfieri R. New hallmark of hepatocellular carcinoma, early hepatocellular carcinoma and high-grade dysplastic nodules on Gd-EOB-DTPA MRI in patients with cirrhosis: a new diagnostic algorithm. Gut 2018;67:1674-82.
36. Hernando D, Cook RJ, Qazi N, Longhurst CA, Diamond CA, Reeder SB. Complex confounder-corrected R2* mapping for liver iron quantification with MRI. Eur Radiol 2021;31:264-75.

Cite this article as: Zheng G, Wei F, Lu P, Yang G, Li C, Lin C, Zhou Y, Chen Y, Tian J, Wang X, Wang L, Liu W, Zhang G, Cai Q, Huang H, Yun Y. IDEAL-IQ measurement can distinguish dysplastic nodule from early hepatocellular carcinoma: a case-control study. Quant Imaging Med Surg 2024. doi: 10.21037/qims-23-1593